



Transient computational fluid dynamics simulation of pulse feed in vacuum membrane distillation process

Jianping Huang^{1,2} · Xiaolong Lu^{1,4} · Xinmiao Zhang³

Received: 22 November 2021 / Revised: 9 March 2022 / Accepted: 21 March 2022 / Published online: 27 May 2022
© The Author(s), under exclusive licence to Springer Nature Switzerland AG 2022

Abstract

Temperature polarization has a significant impact on the efficiency of membrane distillation (MD) systems and leads to a decrease in the overall thermal efficiency and MD flux. To increase the disturbance of the feed near the membrane wall, reduce the adverse effects caused by the temperature polarization, and improve the membrane flux, an innovative vacuum membrane distillation (VMD) operation mode was proposed, in which the traditional steady-state feed is replaced with the pulse feed. Conventional steady-state simulations cannot fully and clearly demonstrate the dynamic changes in the VMD performance parameters over time during the pulse feed. Therefore, a two-dimensional computational fluid dynamics (CFD) transient VMD model was established herein. The simulation results demonstrate that the pulse feed mode could guarantee the operation of the VMD system at a high thermal efficiency and significantly improve the MD flux. Using the optimal pulse parameters, the effects of the pulse feed were more pronounced with a shorter membrane module length and when the feed temperature, velocity, and concentration were higher. The proposed pulse feed mode and transient model is a new approach that can provide a theoretical basis for improving the MD performance, optimizing the operating parameters, and filling the gap in the numerical simulation of MD. The proposed operation mode and simulation method can also be used in the MD process employing composite membranes to study the influence of membrane materials on the MD parameters.

Keywords Pulse feed · Vacuum membrane distillation · Transient model · Numerical simulation

1 Introduction

Membrane distillation (MD) is a novel water treatment technology that combines traditional distillation with modern membrane technology [1]. MD can utilize low-grade thermal sources, such as industrial waste-heat and geothermal or solar energy [2, 3], theoretically afford a desalination efficiency exceeding 99.99%, and realize brine saturation and

crystallization [4, 5]. Therefore, MD has drawn increasing attention as an emerging desalination and zero-liquid discharge technology [6–8]. However, MD has not been widely used in industry, primarily because the series of steps in the MD process requires improvement. The areas to be addressed include hydrophilization leakage of hydrophobic membrane materials, membrane module design and drying methods, process optimization and system integration, phase change heat recovery, and heating and waste-heat utilization [9, 10].

Membrane wetting, membrane fouling, and temperature and concentration polarization are phenomena that can reduce the MD flux, damage membrane materials, and prevent continuous operation of the MD process. To mitigate these undesirable phenomena, the development of novel composite membranes is a research direction that has attracted much attention. Pan et al. [11] prepared composite hydrophobic perfluoropolyether (PFPE)/polyvinylidene fluoride (PVDF) membranes by coating and UV curing and studied the effects of organic and inorganic foulants on the membrane properties in vacuum membrane distillation (VMD). The composite PFPE/PVDF membranes exhibited promising anti-wetting and antifouling properties. Galiano et al. [12]

✉ Xiaolong Lu
13920286131@163.com

¹ State Key Laboratory of Separation Membranes and Membrane Processes, Institute of Biological and Chemical Engineering, School of Material Science and Engineering, Tiangong University, Tianjin 300387, China
² School of Chemical and Environmental Engineering, Anyang Institute of Technology, Anyang 455000, China
³ Beijing Research Institute of Chemical Industry, SINOPEC, Beijing 100013, China
⁴ State Key Laboratory of Membranes Materials and Membrane Applications, Tianjin Motimo Membrane Tech.Co.,Ltd, No.60.11th Street, TEDA, Tianjin 300457, China

developed a novel PVDF-graphene composite membrane. In the direct contact membrane distillation (DCMD) experiment, the membrane showed long-lasting salt rejection and higher stability over time. Jia et al. [13] prepared a polyvinylidene fluoride-co-hexafluoropropylene (PH)-PS composite membrane using a novel hybrid electrospin-electrospray process. The PH-PS composite membrane was characterized by superhydrophobicity, uniform pore distribution, and high porosity, which greatly increased the liquid entry pressure of water. In DCMD, the PH-PS composite membrane still exhibited excellent anti-wetting performance and high salt rejection under harsh feed conditions. Nanocomposite materials have many characteristics that can improve or overcome the weakness of a single material, give full play to the advantages of each material, and confer new properties to the resultant material. Research on novel nanocomposite materials [14–18] can provide directives for the development of membrane materials with superior properties. Computational simulation is another approach for material research. Computational simulation can be used to simulate and analyze the composition, microstructure, and properties of materials. Zhao et al. [19] used a novel neural network approach to quantify the performance indices of piezoresistive nanocomposite materials. Qi and Liu [20] also introduced the application of deep learning and similar computational methodologies in material research.

Vacuum membrane distillation can afford a higher MD flux than other MD processes [21]. Accordingly, the temperature polarization problem is more pronounced in VMD [22]. In the VMD process, the operating conditions have a significant impact on the system performance [23], where comprehensive understanding of this impact is key to the commercial application of MD [24]. Song et al. [25] and Zhang et al. [26] experimentally demonstrated that the MD flux increased with increasing feed temperature. Safavi and Mohammadi [27] and Criscuoli et al. [28] reported that the MD flux increased significantly with increasing feed velocity. Zhang et al. [26] noted that the MD flux decreased with increasing concentration of the non-volatile solute, which reduced the mass transfer driving force.

Other researchers have proposed auxiliary methods for improving the MD performance. For example, Zou et al. [29] and Julian et al. [30] adopted regular air backwashing in a submerged VMD, which reduced membrane scaling and increased the MD flux. Despite achieving improved MD performance, the operations must be paused, so the MD process cannot be executed continuously. Ji et al. [31] utilized a microwave source for the VMD process and investigated the influence of the operating conditions on the process of microwave-enhanced mass transfer. Microwave irradiation could efficiently and uniformly heat the membrane module and dramatically improve the VMD performance. Huang et al. [32] proposed a new method, electric field-assisted VMD, for

mitigating membrane fouling. The best antifouling capability was achieved with an intermittent electric field strength of 1.0 V/cm. Ye et al. [33] introduced microbubble aeration (MBA) in the VMD process, where MBA was applied in the process of high-concentration seawater desalination to alleviate membrane fouling, enhance MD flux, and reduce the effective desalination treatment time. However, additional equipment is required in these processes, which complicates the system.

In recent years, CFD modeling has been widely used in the study of MD hydrodynamic behavior because of its special advantages in flow field visualization [34]. Tang et al. [35] proposed a 2D CFD model of VMD to study the influence of the feed conditions on MD flux and concluded that the MD flux increased with the feed temperature and velocity. Liu et al. [36] applied the CFD model coupled with the momentum, energy, and mass conservation equations to the simulation of the VMD system. However, the influence of the feed concentration on the mass and heat transfer processes was not considered in the model. Using CFD simulations, Zuo et al. [37] optimized the VMD module, where the water production cost of the optimized system was reduced by 38.1%. Anqi et al. [38] conducted 3D transient simulations of VMD modules and investigated the mean values of the local flux, temperature polarization coefficient, and pressure difference under different operating inlet conditions. However, these studies only provided the mean values and distributions of relevant parameters and did not consider dynamic changes in the various parameters over time.

Based on the above analyses, to decrease the adverse effects caused by temperature polarization and improve the MD flux, a novel and feasible operation mode is proposed herein. Specifically, the traditional steady-state feed is replaced by pulse feed to realize continuous, stable, and efficient operation of the VMD. In the proposed pulse feed mode, only one solenoid valve needs to be set on the feed side. Therefore, its process flow is more concise than other strengthening methods. Because the steady-state simulation is not applicable to the pulse feed mode, a 2D transient CFD model based on hollow fiber VMD is established for detailed exploration of the dynamic influence of pulse feed on various VMD performance parameters. Momentum and energy conservation equations are coupled in the transient model, and the influence of fluid oscillation caused by pulse feed on the physical quantities is simultaneously considered. The results can provide a theoretical basis for improving the performance of MD systems and optimizing the operation parameters.

2 Theory

2.1 Governing equations

The governing transport equations are listed in Supplementary Material S1.

2.2 Mass and heat transfer

Three fundamental transfer mechanisms are involved in the MD process: Knudsen diffusion, molecular diffusion, and Poiseuille flow [39, 40]. For VMD, Knudsen diffusion and Poisson flow are more suitable than molecular diffusion because of the low partial pressure of air in the membrane pores [41]. The Knudsen number ($Kn = l/d_p$) can be used to determine the dominant mechanism ($Kn < 0.01$, Poiseuille flow; $0.01 < Kn < 1$, Poiseuille flow–Knudsen diffusion; $Kn > 1$, Knudsen diffusion), where l and d_p are the mean free-path and the mean pore diameter, respectively.

The hydrophobic polyvinylidene fluoride (PVDF) membrane used in this study was produced by our research group [42, 43]. The properties of the PVDF membranes used herein are listed in Table 1. Within the studied temperature range (333.15–353.15 K), l is greater than 2.80 μm [41]. The calculated Kn value was greater than 17.50. Therefore, the dominant mechanism is Knudsen diffusion.

The mass and heat transfer equations are listed in Supplementary Material S2.

2.3 Geometry model and grid generation

In the present study, five PVDF hollow fibers were packaged in the module and the feed flowed in parallel on the lumen side; the subsequent experiments and CFD models are based on this structure.

Simplifying the multi-fiber module into a single-fiber module significantly reduces tedious calculations [39]. Therefore, the following simplifying assumptions are proposed for the model: (1) the membrane surface roughness is neglected, (2) the membrane wall is set to be rigid and is unaffected by the feed flow, (3) the physical properties of the feed remain constant irrespective of changes in the concentration near the membrane surface due to water evaporation, and (4) irrespective of heat loss, the outlet temperature is only related to evaporation. Based on the above assumptions, a 2D CFD model of a single-fiber hot channel was established, as shown in Fig. 1a.

Table 1 Membrane properties

Hollow fiber membrane module	Values
Effective length of fibers (mm)	200/400/600/1000
Shell diameter (mm)	8
Number of fibers	5
Inner diameter of fibers (mm)	0.8
Outer diameter of fibers (mm)	1.1
Porosity (%)	85
Mean pore size (μm)	0.16
Liquid entry pressure of water (kPa)	350

A structured quadrilateral meshing method was adopted, and the meshes near the membrane surface were refined to obtain accurate results.

2.4 Boundary conditions

Feed inlet: The feed velocity at steady-state feed was varied from 0.60 to 1.20 m s^{-1} , and the feed velocity at the pulse feed was defined by user-defined functions (UDFs). The feed temperatures were 333.15, 343.15, and 353.15 K.

Feed outlet: The feed outlet was set to the pressure-outlet; the relative pressure was set to 0 MPa.

Vacuum export: The vacuum export was set to the pressure-outlet; the vacuum degree was -0.090 MPa.

Membrane surface: The membrane surface was set as a no-slip wall.

The mass and energy source terms were loaded for the membrane surface and the computational domain on both sides of the membrane wall and set by UDFs, as presented in Eqs. (S1-1)–(S1-7).

3 Experimental and pulse parameters

3.1 Experimental procedure

The experimental setup for the VMD is shown in Fig. 1b. The feed stream was heated to the set temperature and then circulated using a feed pump. The feed rate was adjusted by a control valve set at the pump outlet. The feed rate was determined using a flow gauge set on the pipeline. A solenoid valve was arranged between the control valve and flow meter to generate pulse feed (the solenoid is normally open for steady feed). The permeate side was evacuated to produce a negative pressure (constant at 0.090 MPa) using a vacuum pump. The evacuated vapor was weighed after condensation. The temperatures of the feed inlet, outlet, and vacuum outlet were monitored using a thermometer.

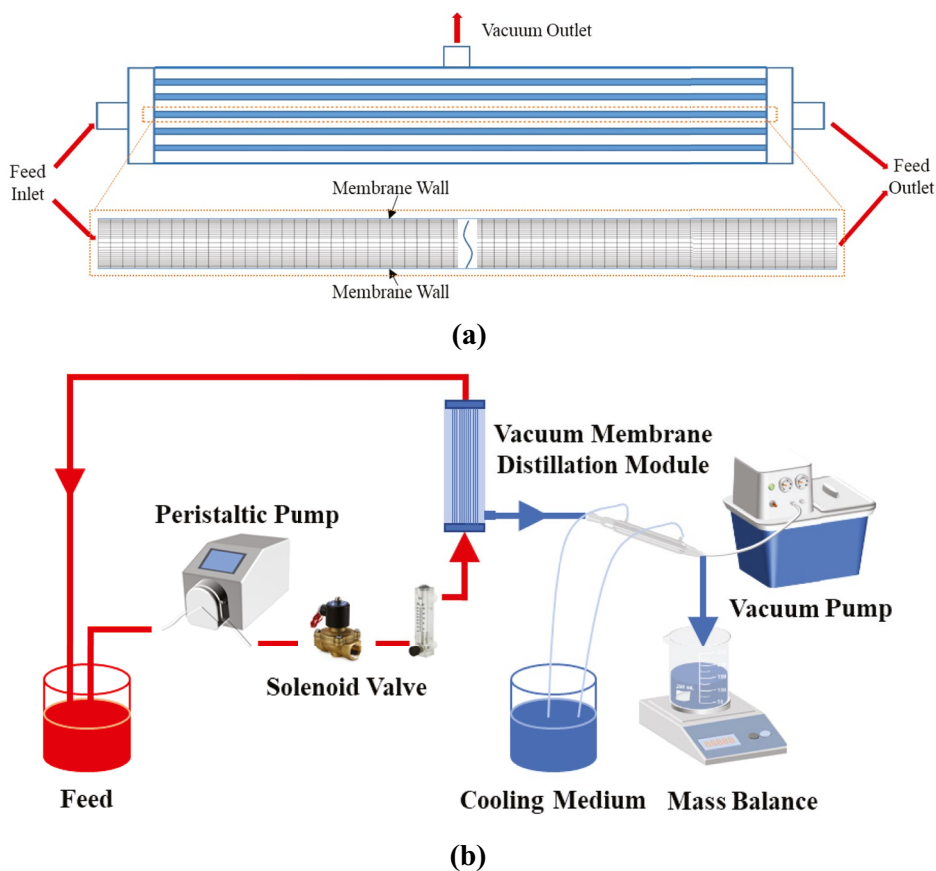
3.2 Feed solution

In the verification experiments, distilled water was used as the feed, while aqueous NaCl of different concentrations was used as the feed solution in the CFD simulation. The mole fractions of NaCl in the feed solution were 0.015, 0.029, 0.044, and 0.058, respectively.

3.3 Pulse parameters

The pulse parameters used in the simulation were the pulse period (Pp) and pulse interval (Pi). Pp and Pi are the times

Fig. 1 **a** Domain and meshes of the 2D CFD model. **b** Experimental setup of VMD



when the solenoid valve is set to open and shut in a pulse cycle (P_c), respectively. P_c is the sum of P_p and P_i , as shown in Fig. 2.

4 Results and discussion

4.1 Model validation

The simulated values of the outlet temperature and MD flux at different feed velocities and temperatures were compared

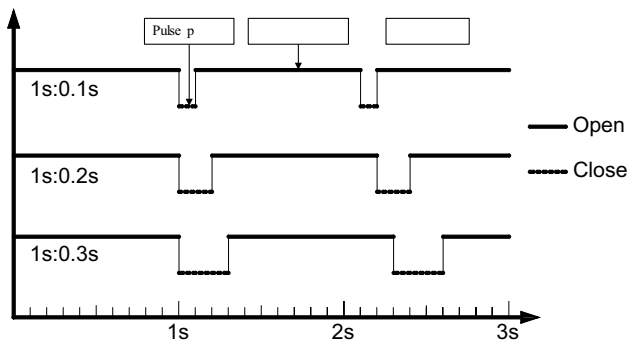


Fig. 2 Schematic of pulse parameters

with the experimental data to verify the accuracy of the CFD model (Fig. 3). The simulation results and experimental data are in good agreement. This indicates that the proposed CFD model exhibited good reliability and can provide an accurate prediction of the VMD system performance.

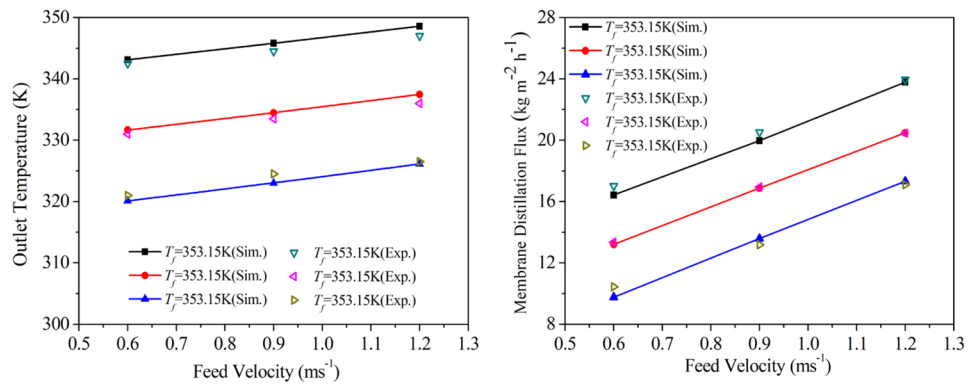
4.2 Effect of pulse parameters

In this section, the MD flux is taken as the target quantity, and the effect of the pulse parameters is analyzed to determine the optimal pulse period (P_p) and pulse interval (P_i).

4.2.1 Determination of P_p

A series of transient calculations was performed with the same pulse interval ($P_i = 1$ s) and different pulse periods ($P_p = 0.05, 0.1, 0.2, 0.3$ s). The optimal pulse period was determined by comparing the mean MD flux in one pulse cycle ($P_c = P_i + P_p$) after the solenoid valve was opened, as shown in Fig. 4a. When P_p was 0.1 s, the mean MD flux was the largest. While closing the solenoid valve, the tube-side fluid maintained a certain motion velocity under the action of inertial force. After the solenoid valve was opened, the fluid velocity rapidly returned to its initial value. When P_p was 0.05 s, the time taken to close the solenoid valve was

Fig. 3 Comparison of experimental data and simulation results at different feed velocities and temperatures ($L = 200$ mm)



extremely short; thus, the fluid velocity changed little in one pulse cycle, and the disturbance to the feed near the wall was also slight. Although the membrane flux was higher than that of the steady-state feed, it was still less than the membrane flux when Pp was 0.1 s. When Pp was greater than 0.1 s, the time required to close the solenoid valve was extremely long. While closing the solenoid valve, the fluid velocity is greatly reduced (almost zero) owing to the wall shear force. For VMD, the membrane flux decreases with a decrease in the fluid velocity; therefore, when Pp is larger, the fluid remains in the low-velocity state for a longer period, and the membrane flux becomes smaller. According to the above analysis, the optimal pulse period was 0.1 s.

4.2.2 Determination of Pi

A series of transient calculations was performed using the model with the same pulse period ($Pp = 0.1$ s) and different pulse intervals ($Pi = 0.5, 1.0, 2.0, 3.0$ s). Figure 4b shows the variation in the MD flux in one pulse cycle with different

pulse intervals. When Pi was 1 s, the average MD flux was the highest. When the solenoid valve was closed, the fluid velocity decreased. After the solenoid valve was opened, the fluid velocity gradually recovered. When Pi was 0.5 s, the solenoid valve was closed before the fluid velocity recovered to the initial value, which caused the fluid to flow at a rate below the feed velocity. Although the MD flux could be improved, it was less than the membrane flux when Pi was 1 s. When Pi was greater than 1 s, the fluid velocity recovered to its initial value during the period in which the solenoid valve was being opened, and the operating state was the same as that of the steady-state feed. Therefore, when Pi is larger, the MD process is closer to the steady-state feed state, and the increase in the MD flux is less pronounced. Therefore, the optimal pulse interval was determined to be 1 s. Overall, the optimal pulse parameters were $Pp = 0.1$ s and $Pi = 1$ s, and the subsequent analyses were based on this set of pulse parameters. Notably, in the subsequent simulation, steady-state feed was performed for 0–1 s, and the solenoid valve was closed in the time period of 1–1.1 s, opened at 1.1 s, and remained open until 2.1 s. The period of 1–2.1 s is a pulse cycle, and the next pulse cycle is executed at 2.1 s.

4.3 Effect of inlet temperature

In this section, the effects of the inlet temperature on the VMD heat and mass transfer performance are compared and analyzed under steady-state and pulse feed conditions ($Pi = 1$ s, $Pp = 0.1$ s). Table 2 shows the results of simulation of the steady-state feed at different feed temperatures.

Figure 5a and b show the temperature difference ($\Delta T = T_f - T_{fm}$) and TPC over time at different feed temperatures. The feed bulk and membrane surface temperature decreased during the closing period of the solenoid valve (1–1.1 s) because of the heat lost by water vaporization, but increased gradually as the feed entered the system after the solenoid valve was opened at 1.1 s. However, the temperature of the membrane surface increased later than that of the feed bulk temperature; thus, ΔT increased and TPC decreased in the preliminary stage. As the flow

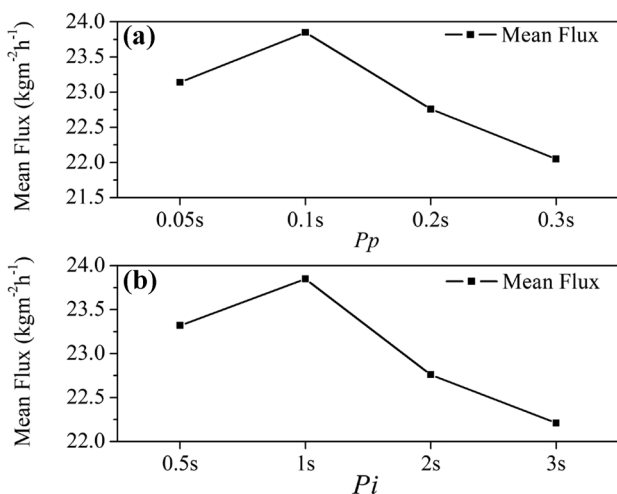


Fig. 4 Variation of mean membrane flux in one pulse cycle **a** with different pulse periods ($Pi = 1.0$ s), **b** with different pulse intervals ($Pp = 0.1$ s), $V_f = 1.20$ m s⁻¹, $T_f = 353.15$ K, $x_{NaCl} = 0.029$

Table 2 Results of simulation of steady-state feed at different feed temperatures ($V_f = 1.20 \text{ m s}^{-1}$, $x_{\text{NaCl}} = 0.029$)

T_f (K)	ΔT (K)	TPC	Q_f (Wm ⁻²)	h_f (Wm ⁻² K ⁻¹)	η (%)	J (kg m ⁻² h ⁻¹)
333.15	3.82	0.9884	25312.38	6626.28	79.04	10.67
343.15	5.37	0.9842	38928.39	7249.23	86.56	14.53
353.15	6.59	0.9811	51464.09	7809.42	94.90	18.03

field gradually stabilized on the lumen side, ΔT and TPC gradually stabilized. Moreover, the TPC value was higher than that at steady-state because the membrane surface temperature increased due to oscillation and mixing of the fluid. As shown in Fig. 5a and b, the higher the feed temperature, the greater the change in ΔT , and the greater the increase in TPC.

As the membrane surface temperature increased, the transmembrane vapor pressure difference and the mass transfer driving force increased. Therefore, from Eqs. (S2-1) and (S2-2), it can be deduced that the normalized membrane flux (N) increased, as shown in Fig. 5c. Figure 5d and e display the variation in the heat flux (Q_f) and convective heat transfer coefficient (h_f) over time. The membrane surface temperature had little effect on the evaporation enthalpy, and according to Eq. (S2-8), Q_f increases as J increases. Thus, oscillation mixing of the feed caused a strong disturbance of the fluid near the wall and destroyed the thermal boundary layer, thereby increasing h_f . According to Eq. (S2-9), h_f is affected by both Q_f and ΔT . Compared with the system employing steady-state feed, Q_f increased and ΔT decreased in the system with pulse feed; therefore, h_f increased in the latter. As the feed temperature increased, h_f increased.

In the period where the solenoid valve was being closed, because the heat was removed by water vaporization, T_{fm} and T_{out} decreased and ΔT_f increased. Therefore, according to Eq. (S2-13), η decreased, as shown in Fig. 5f. After the solenoid valve was opened, with the recovery of the temperature field, the membrane flux, the membrane surface temperature, and the outlet temperature gradually increased, and η also increased. However, η did not recover to the steady-state value because of the effect caused by closing the solenoid valve. As the feed temperature increased, the value of η after being restored was closer to the steady-state value.

The increase in TPC became more pronounced with the feed temperature in the pulse feed system. Therefore, at a higher feed temperature, the pulse feed mode is more conducive to reducing the adverse effect of temperature polarization. Consequently, the VMD system consistently delivered higher thermal efficiency and MD flux.

4.4 Effect of inlet velocity

The influence of the feed velocity on the VMD performance was compared and analyzed under steady-state feed and

pulse feed ($P_i = 1 \text{ s}$, $P_p = 0.1 \text{ s}$) conditions. The simulated data for the steady-state feed system at different feed velocities are listed in Table 3.

Figure 6a and b show the variation in ΔT and TPC over time at different feed velocities. The impact of fluid oscillation (caused by the pulse feed) on the flow field intensified as the feed velocity increased. At higher feed velocity, the bulk feed was mixed more thoroughly with the feed near the membrane wall; thus, ΔT decreased to a greater extent. By comparing Figs. 5a and 6a, it is deduced that ΔT increased from 1.58 and 1.71 to 2.73 K with an increase in the feed temperature and velocity, respectively. When ΔT was larger, the wall temperature was closer to the feed bulk temperature, which indicates that the feed velocity had a greater effect on ΔT than the feed temperature. As seen in Fig. 6b, at the pulse feed, TPC at different feed velocities was greater than the steady-state value, TPC increased to a greater extent with the feed velocity, and the recovery time for the TPC was inversely proportional to the feed velocity. Therefore, increasing the feed velocity can reduce the TPC recovery time and enable the VMD to operate at a higher TPC for a long time.

More complete feed mixing in the lumen side caused by feed oscillation at a higher feed velocity led to a smaller ΔT and higher wall temperature, and thus a greater increase in N (Fig. 6c). The thermal boundary layer was affected by the feed velocity. The thickness of the thermal boundary layer and the thermal resistance decreased as the feed velocity increased. Therefore, the increase in Q_f and h_f became more pronounced with increasing feed velocity (Fig. 6d, e).

As shown in Table 3, under steady-state feed conditions, as the feed velocity increased, η decreased, which is consistent with the conclusion of a prior study [44]. The increase in the feed velocity (V_f) led to an increase in $J/\Delta T_f$, but $J/\Delta T_f$ increased to a lesser extent than V_f . Therefore, according to Eq. (S2-13), η decreased with an increase in the feed velocity. At the pulse feed, the time required to reestablish the thermal boundary layer and the recovery time of the flow field in the lumen side became longer as the feed velocity decreased. Consequently, a smaller η was associated with a longer recovery time for η , as seen in Fig. 6f.

4.5 Effect of feed concentration

Table 4 displays the simulated data for the steady-state feed with different feed concentrations. As summarized in

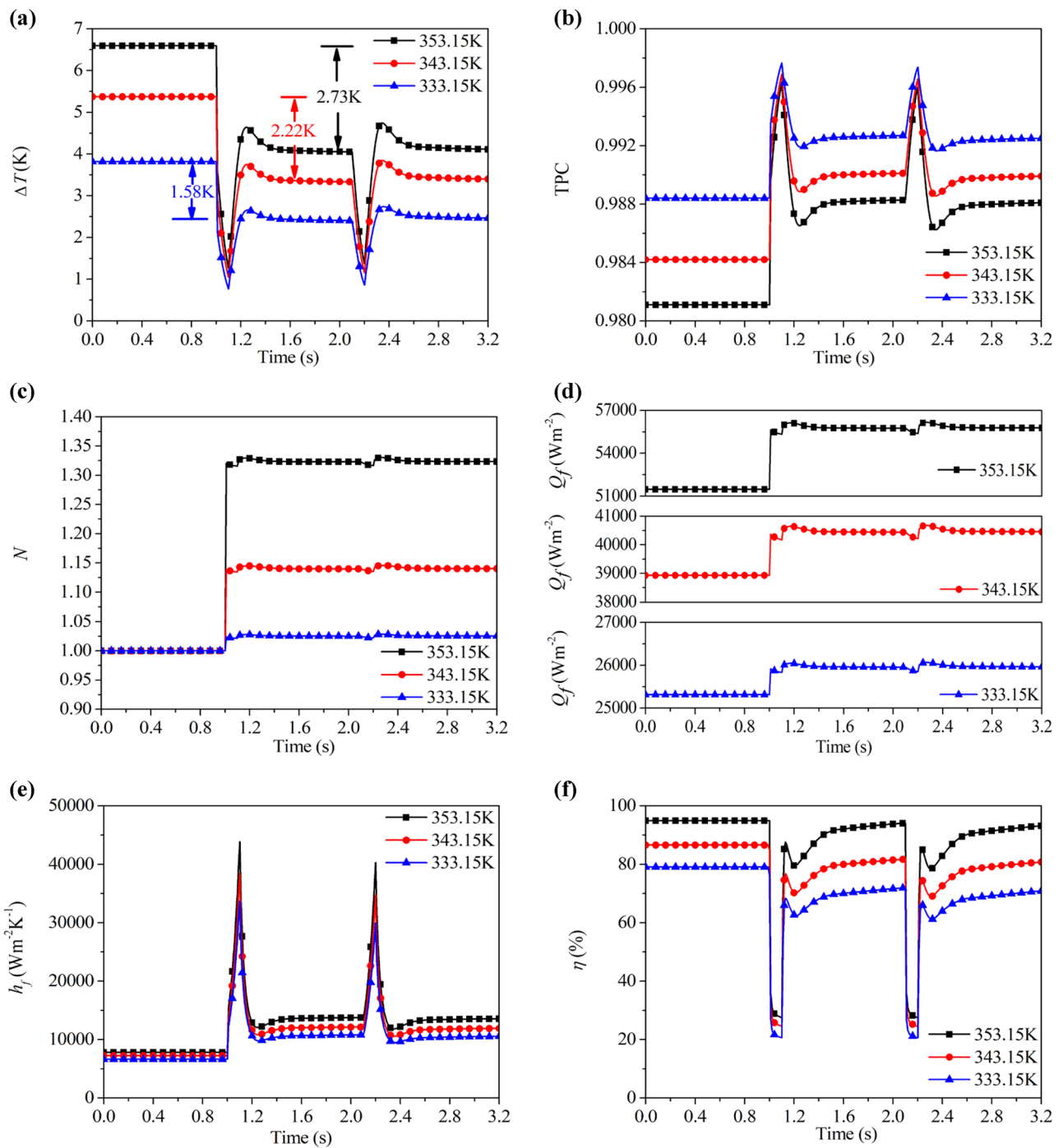


Fig. 5 Variation of **a** ΔT , **b** TPC, **c** N , **d** Q_f , **e** h_f , and **f** η over time at different feed temperatures ($V_f = 1.20 \text{ m s}^{-1}$, $x_{NaCl} = 0.029$, $Pp = 0.1 \text{ s}$, $Pi = 1.0 \text{ s}$)

Table 4, ΔT , Q_f , and J decreased with an increase in the feed concentration under steady-state feed conditions, while TPC, h_f , and η increased. When the feed concentration in

the pulse feed was higher, the MD flux increased gradually, as shown in Fig. 7. The fluid kinematic viscosity increased with increasing feed concentration; therefore, the formed

Table 3 Simulated data for steady-state feed at different feed velocities ($T_f = 353.15 \text{ K}$, $x_{NaCl} = 0.029$)

V_f (ms^{-1})	ΔT (K)	TPC	Q_f (Wm^{-2})	h_f ($Wm^{-2} K^{-1}$)	η (%)	J ($kg \text{ m}^{-2} \text{ h}^{-1}$)
0.60	4.43	0.9872	24845.85	5608.54	96.60	10.65
0.90	5.43	0.9844	37995.64	6997.36	95.75	13.88
1.20	6.59	0.9811	51464.09	7809.42	94.90	18.03

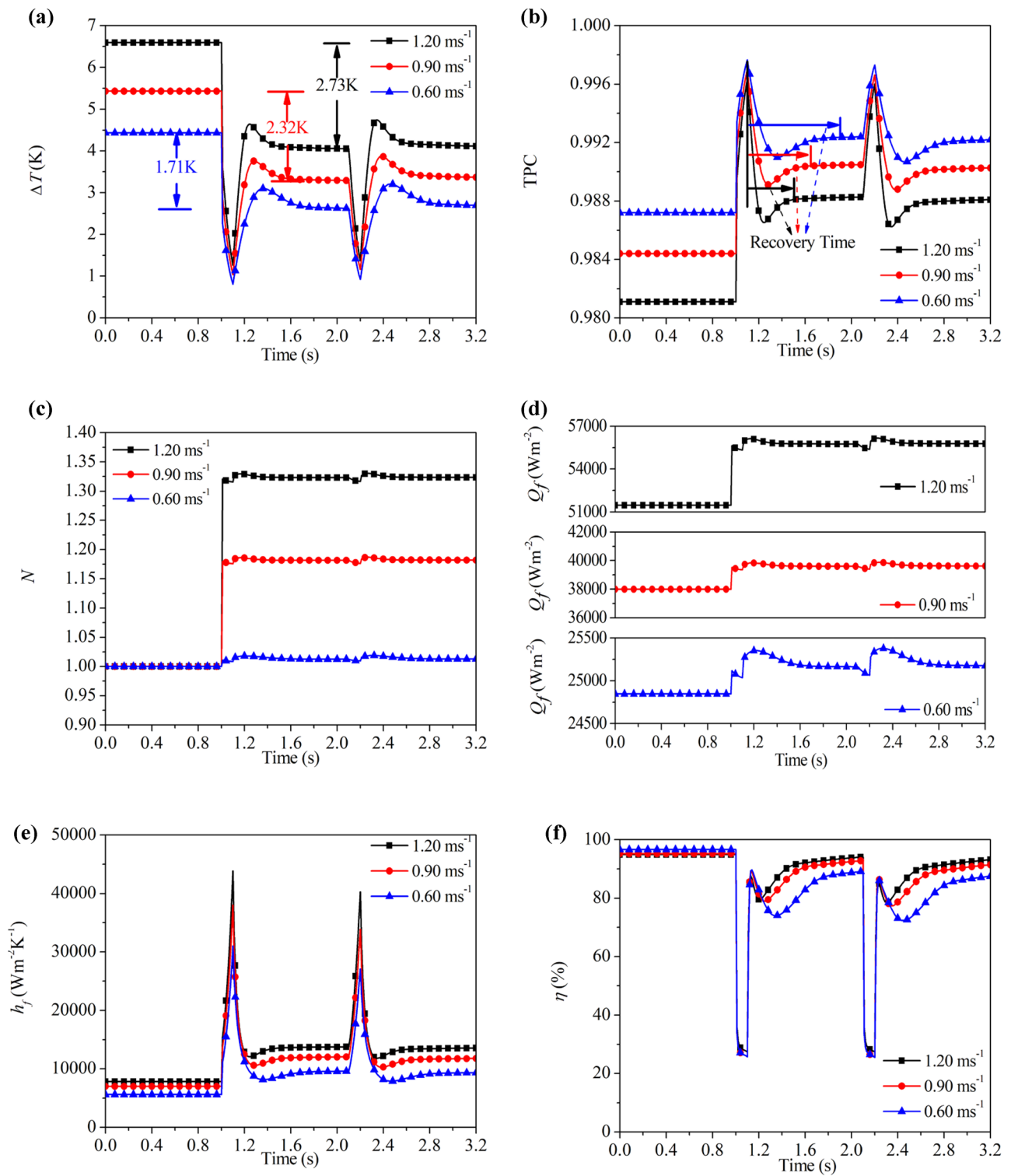


Fig. 6 Variation of **a** ΔT , **b** TPC, **c** N , **d** Q_f , **e** h_f , and **f** η over time at different feed velocities ($T_f = 353.15$ K, $x_{\text{NaCl}} = 0.029$, $Pp = 0.1$ s, $Pi = 1.0$ s)

Table 4 Simulated data for steady-state feed at different feed concentrations ($T_f = 353.15$ K, $V_f = 1.20$ m s⁻¹)

x_{NaCl}	$\Delta T/(K)$	TPC	$Q_f/(Wm^{-2})$	$h_f/(Wm^{-2} K^{-1})$	$\eta(\%)$	$J/(kg m^{-2} h^{-1})$
0.015	6.94	0.9800	53853.63	7720.98	93.98	21.18
0.029	6.59	0.9811	51464.09	7809.42	94.90	18.03
0.044	6.23	0.9821	49131.12	7886.22	96.21	16.04
0.058	5.86	0.9832	46855.88	7995.88	96.50	15.08

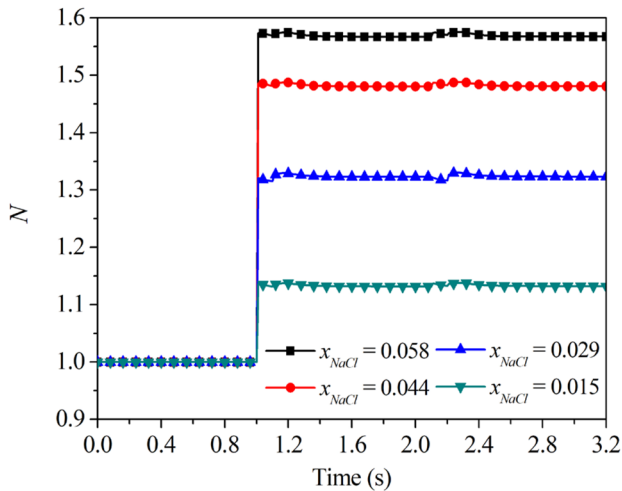


Fig. 7 Variation of N over time with different feed velocities ($T_f = 353.15$ K, $V_f = 1.20$ m s⁻¹, $Pp = 0.1$ s, $Pi = 1.0$ s)

boundary layer was thicker at higher feed concentrations. However, fluid oscillation can reduce the thickness of the boundary layer and the heat and mass transfer resistance. The stronger influence of the pulse feed on the boundary layer formed by the high-concentration feed increases the membrane flux. Therefore, pulse feed is more conducive to the treatment of high-concentration feed.

4.6 Effect of module length

The MD module used in industry is usually 400–1000 mm in length. The influence of the module length on the VMD performance under pulse feed conditions was investigated

Table 5 Simulated data for steady-state feed with different module lengths ($T_f = 353.15$ K, $V_f = 1.20$ m s⁻¹)

$L/(mm)$	$\Delta T/(K)$	TPC	$Q_f/(Wm^{-2})$	$h_f/(Wm^{-2} K^{-1})$	$\eta(\%)$	$J/(kg m^{-2} h^{-1})$
200	6.59	0.9811	51464.09	7809.42	94.90	18.03
400	8.90	0.9463	56194.97	6314.04	91.94	16.28
600	10.69	0.8838	59176.09	5535.65	87.91	14.17
1000	12.94	0.8571	62304.52	4814.88	85.85	13.38

for module lengths of 200, 400, 600, and 1000 mm. The simulated data for the steady-state feed with different module lengths (L) are summarized in Table 5.

Under steady-state feed conditions, the fluid velocity in the lumen side remained constant, and the boundary layer thickness gradually increased along with the fiber length. The longer the module, the thicker the boundary layer in the rear section of the module. At the same time, because the heat was removed by water evaporation, the temperature in the rear section of the module was lower than that of the inlet section. Therefore, the MD flux gradually decreased along the fiber. In the case of pulse feed, the fluid oscillation could destroy the boundary layer, especially in the rear section of the module. Thus, a higher MD flux can be obtained with pulse feed than in the case of steady-state feed.

Figure 8 shows the variation of N with different module lengths over the course of 0–7.6 s. The data in Fig. 8 show that (1) a shorter module length led to a greater increase in the MD flux under pulse feed conditions, and (2) the longer the module length, the weaker the periodic change in the MD flux. This is because of the short residence time of the feed in the shorter module, which enabled the fluid velocity to recover quickly after the solenoid valve was opened. However, because the boundary layer recovered later than the bulk velocity, and the heat and mass transfer resistance were still small, the MD flux increased further. In the longer module, the fluid velocity did not fully recover at the beginning of the next pulse cycle, causing the fluid in the module to flow below the feed velocity. However, the boundary layer was destroyed and thinned because of the fluid oscillation, which reduced the heat and mass transfer resistance, causing the MD flux of the longer module to be higher than that under steady-state feed conditions. However, the increase in the flux was less than that in the shorter module.

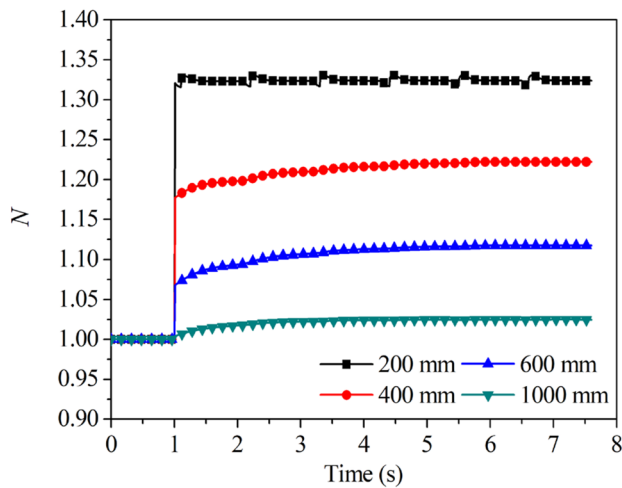


Fig. 8 Variation of N with different module lengths over course of 0–7.6 s ($T_f = 353.15$ K, $V_f = 1.20$ m s⁻¹, $Pp = 0.1$ s, $Pi = 1.0$ s)

5 Conclusion

The pulse feed mode was introduced into the VMD for the first time. The improved process can reduce the adverse effects of temperature polarization on the VMD performance and improve the MD flux. The VMD process with pulse feed mode can realize the simultaneous operation and pipeline cleaning without being suspended. The improved process does not require a lot of auxiliary equipment and is more economical, and this method can provide a new idea for the industrial application of VMD process. Because the steady-state simulation was not applicable to the pulse feed mode proposed in this study, a 2D transient CFD model was established. This transient model can comprehensively demonstrate dynamic changes in various performance parameters over time in the pulse feed VMD process. The optimal pulse parameters ($Pi = 1$ s, $Pp = 0.1$ s) were determined by comparing and analyzing the MD flux in a pulse cycle. On this basis, the effects of the feed condition and module dimensions on the VMD performance were analyzed. The simulation results showed that the pulse feed mode could significantly improve the MD flux, and the effect of the pulse feed was better at higher feed temperatures, velocities, and concentrations, and with shorter membrane modules. The results of this study can provide a theoretical basis for optimizing the VMD performance and a new strategy for VMD scale-up applications. The effect of composite materials on the MD performance under different operating conditions can be studied by introducing a pulse feed mode into the MD process based on a composite material membrane. By modeling the characteristic parameters of the composite materials, the hydrophobicity and antifouling properties of the composite materials can be analyzed, and the MD flux and salt rejection can be predicted.

Nomenclature A_{eff} : The effective membrane area (m²); B : MD coefficient (kg/(m² s Pa)); C_p : Specific heat capacity of feed (J/(kg K)); d_p : The mean pore diameter of the hydrophobic membrane (m); g : The gravitational acceleration (m/s²); J : The transmembrane mass flux (kg/(m² h)); k : The heat conductivity (W/(m K)); Kn : Knudsen number; l : The mean free-path of the transported gas molecules through the membrane pores (m); M_{NaCl} : The molecular mass of NaCl (kg/mol); M_{water} : The molecular mass of water (kg/mol); N : The normalized flux; P_{vapor} : The saturated vapor pressure at the feed-membrane interface (Pa); P_{vacuum} : The vacuum pressure of permeate side (Pa); P^s : The saturated vapor pressure (Pa); Pp : Pulse period (s); Pi : Pulse interval (s); Pc : Pulse cycle (s); Q_v : The latent heat related to the evaporation (W/m²); Q_c : The transmembrane heat conduction (W/m²); R : Universal gas constant (J/(mol K)); S_m : The mass source term (kg/(m³ s)); S_{mom} : The momentum source term (N/m³); S_h : The heat source term (W/(m³ s)); T : Temperature (K); \vec{v} : Velocity vector; V_f : Feed velocity (m/s); w_{NaCl} : The mass of NaCl in the feed (kg); w_{water} : The mass of water in the feed (kg); x : The mole fraction; α : The activity coefficient; δ : The thickness of the membrane (m); ε : The porosity of the membrane (%); μ : Viscosity (Pa s); ρ : Density (kg/m³); τ : The tortuosity factor of the pores; ΔH_v : The latent heat of water vapor (J/kg); ΔT : The temperature difference of the feed bulk and membrane wall; ΔT_f : The temperature drop of the feed along the fiber (K); ∇ : Hamiltonian operator; ∇P : Divergence of the stress tensor; ∇^2 : Laplacian vector

Supplementary information The online version contains supplementary material available at <https://doi.org/10.1007/s42114-022-00502-6>.

Funding This work was supported by the Program for Innovative Research Team in University of Tianjin (grant number TD13-5044), the National Key Research and Development Plan (grant number 2017YFC0403902), and the Program for Changjiang Scholars and Innovative Research Team in University (PCSIRT) of Ministry of Education of China (grant number IRT17_R80).

Declarations

Conflict of interest The authors declare no competing interests.

References

- Wang L, Wang HT, Li BA et al (2014) Novel design of liquid distributors for VMD performance improvement based on cross-flow membrane module. *Desalination* 336:80–86. <https://doi.org/10.1016/j.desal.2014.01.004>
- Lokare OR, Tavakkoli S, Rodriguez G et al (2017) Integrating membrane distillation with waste heat from natural gas compressor stations for produced water treatment in Pennsylvania. *Desalination* 413:144–153. <https://doi.org/10.1016/j.desal.2017.03.022>
- Tan YZ, Wang H, Han L et al (2018) Photothermal-enhanced and fouling-resistant membrane for solar-assisted membrane distillation. *J Membr Sci* 565:254–265. <https://doi.org/10.1016/j.memsci.2018.08.032>
- Liao Y, Zheng GT, Huang JHJ et al (2020) Development of robust and superhydrophobic membranes to mitigate membrane scaling and fouling in membrane distillation. *J Membr Sci* 601:117962. <https://doi.org/10.1016/j.memsci.2020.117962>
- Warsinger DM, Swarninathan J, Guillen-Burrieza E et al (2015) Scaling and fouling in membrane distillation for desalination applications: a review. *Desalination* 356:294–313. <https://doi.org/10.1016/j.desal.2014.06.031>
- Schwantes R, Chavan K, Winter D et al (2018) Techno-economic comparison of membrane distillation and MVC in a zero liquid

- discharge application. *Desalination* 428:50–68. <https://doi.org/10.1016/j.desal.2017.11.026>
7. Semblante GU, Lee JZ, Lee LY et al (2018) Brine pre-treatment technologies for zero liquid discharge systems. *Desalination* 441:96–111. <https://doi.org/10.1016/j.desal.2018.04.006>
 8. Lu KJ, Cheng ZL, Chang J et al (2019) Design of zero liquid discharge desalination (ZLDD) systems consisting of freeze desalination, membrane distillation, and crystallization powered by green energies. *Desalination* 458:66–75. <https://doi.org/10.1016/j.desal.2019.02.001>
 9. Lu XL, Wu CR, Gao QJ et al. (2012) Progress in membrane distillation. In: Proceedings of the Fifth National Symposium on the Application of Membrane Separation Technology in the Pharmaceutical Industry
 10. Wang P, Teoh MM, Chung TS (2011) Morphological architecture of dual-layer hollow fiber for membrane distillation with higher desalination performance. *Water Res* 45:5489–5500. <https://doi.org/10.1016/j.watres.2011.08.012>
 11. Pan J, Zhang F, Wang Z et al (2022) Enhanced anti-wetting and anti-fouling properties of composite PFPE/PVDF membrane in vacuum membrane distillation. *Sep Purif Technol* 282:120084. <https://doi.org/10.1016/j.seppur.2021.120084>
 12. Grasso G, Galiano F, Yoo MJ et al (2020) Development of graphene-PVDF composite membranes for membrane distillation. *J Memb Sci* 604:118017. <https://doi.org/10.1016/j.memsci.2020.118017>
 13. Jia W, Kharraz JA, Guo J (2020) Alicia Kyoungjin An, Superhydrophobic (polyvinylidene fluoride-co-hexafluoropropylene)/(polystyrene) composite membrane via a novel hybrid electrospin-electrospray process. *J Memb Sci* 611:118360. <https://doi.org/10.1016/j.memsci.2020.118360>
 14. Han Wu, Zhong Y, Tang Y et al (2021) Precise regulation of weakly negative permittivity in $\text{CaCu}_3\text{Ti}_4\text{O}_{12}$ metacomposites by synergistic effects of carbon nanotubes and grapheme. *Adv Compos Hybrid Mater*. <https://doi.org/10.1007/s42114-021-00378-y>
 15. Qi G, Liu Y, Chen L et al (2021) Lightweight $\text{Fe}_3\text{C}@\text{Fe}/\text{C}$ nanocomposites derived from wasted cornstalks with high-efficiency microwave absorption and ultrathin thickness. *Adv Compos Hybrid Mater* 4:1226–1238. <https://doi.org/10.1007/s42114-021-00368-0>
 16. Jiang Guo Xu, Liu LH (2021) Tunable magnetoresistance of core-shell structured polyaniline nanocomposites with 0-, 1-, and 2-dimensional nanocarbons. *Adv Compos Hybrid Mater* 4:51–64. <https://doi.org/10.1007/s42114-021-00211-6>
 17. Guo J, Chen Z, Abdul W (2021) Tunable positive magnetoresistance of magnetic polyaniline nanocomposites. *Adv Compos Hybrid Mater* 4:534–542. <https://doi.org/10.1007/s42114-021-00242-z>
 18. Jiang Guo Xu, Li ZC (2021) Magnetic $\text{NiFe}_2\text{O}_4/\text{polypyrrole}$ nanocomposites with enhanced electromagnetic wave absorption. *J Mater Sci Technol* 108:64–72. <https://doi.org/10.1016/j.jmst.2021.08.049>
 19. Zhao L, Tallman T, Lin G (2021) Spatial damage characterization in self-sensing materials via neural network-aided electrical impedance tomography: a computational study. *ES Mater Manuf* 12:78–88. <https://doi.org/10.30919/esmm5f919>
 20. Qi Y, Liu C (2021) Deep learning for medical materials: review and perspective. *ES Mater Manuf* 12:17–28. <https://doi.org/10.30919/esmm5f426>
 21. Boonthanon S, Hwan LS, Vigneswaran S et al (1991) Application of pulsating cleaning technique in crossflow microfiltration. *Filtr Sep* 28:199–201. [https://doi.org/10.1016/0015-1882\(91\)80076-H](https://doi.org/10.1016/0015-1882(91)80076-H)
 22. Schofield RW, Fane AG, Fell CJD et al (1990) Factors affecting flux in membrane distillation. *Desalination* 77:279–294. [https://doi.org/10.1016/0011-9164\(90\)85030-E](https://doi.org/10.1016/0011-9164(90)85030-E)
 23. Abu-Zeid MAER, Zhang Y, Dong H et al (2015) A comprehensive review of vacuum membrane distillation technique. *Desalination* 356:1–14. <https://doi.org/10.1016/j.desal.2014.10.033>
 24. Cheng DJ, Li N, Zhang JH (2018) Modeling and multi-objective optimization of vacuum membrane distillation for enhancement of water productivity and thermal efficiency in desalination. *Chem Eng Res Des* 132:697–713. <https://doi.org/10.1016/j.cherd.2018.02.017>
 25. Song LM, Li BA, Sirkar KK et al (2007) Direct contact membrane distillation-based desalination: novel membranes, devices, larger-scale studies, and a model. *Ind Eng Chem Res* 46:2307–2323. <https://doi.org/10.1021/ie0609968>
 26. Zhang L, Wang YF, Cheng LH et al (2012) Concentration of lignocellulosic hydrolyzates by solar membrane distillation. *Biores Technol* 123:382–385. <https://doi.org/10.1016/j.biortech.2012.07.064>
 27. Safavi MA, Mohammadi T (2009) High-salinity water desalination using VMD. *Chem Eng J* 149:191–195. <https://doi.org/10.1016/j.cej.2008.10.021>
 28. Criscuoli A, Carnevale MC, Drioli E et al (2008) Evaluation of energy requirements in membrane distillation. *Chem Eng Process* 47:1098–1105. <https://doi.org/10.1016/j.cep.2007.03.006>
 29. Zou T, Dong XL, Kang GD et al (2018) Fouling behavior and scaling mitigation strategy of CaSO_4 in submerged vacuum membrane distillation. *Desalination* 425:86–93. <https://doi.org/10.1016/j.desal.2017.10.015>
 30. Julian H, Ye Y, Li HY et al (2018) Scaling mitigation in submerged vacuum membrane distillation and crystallization (VMDC) with periodic air-backwash. *J Membr Sci* 547:19–33. <https://doi.org/10.1016/j.memsci.2017.10.035>
 31. Ji ZG, Wang J, Hou DY et al (2013) Effect of microwave irradiation on vacuum membrane distillation. *J Membr Sci* 429:473–479. <https://doi.org/10.1016/j.memsci.2012.11.041>
 32. Huang QL, Liu H, Wang YF et al (2018) A hybrid electric field assisted vacuum membrane distillation method to mitigate membrane fouling. *RSC Adv* 8:18084–18092. <https://doi.org/10.1039/C8RA02304B>
 33. Ye YB, Yu SL, Hou LA et al (2019) Microbubble aeration enhances performance of vacuum membrane distillation desalination by alleviating membrane scaling. *Water Res* 149:588–595. <https://doi.org/10.1016/j.watres.2018.11.048>
 34. Yu H, Yang X, Wang R et al (2012) Analysis of heat and mass transfer by CFD for performance enhancement in direct contact membrane distillation. *J Membr Sci* 405–406:38–47. <https://doi.org/10.1016/j.memsci.2012.02.035>
 35. Tang N, Zhang HJ, Wang W (2011) Computational fluid dynamics numerical simulation of vacuum membrane distillation for aqueous NaCl solution. *Desalination* 274:120–129. <https://doi.org/10.1016/j.desal.2011.01.078>
 36. Liu J, Wang Q, Han L et al (2017) Simulation of heat and mass transfer with cross-flow hollow fiber vacuum membrane distillation: the influence of fiber arrangement. *Chem Eng Res Des* 119:12–22. <https://doi.org/10.1016/j.cherd.2017.01.013>
 37. Zuo GZ, Guan GQ, Wang R (2014) Numerical modeling and optimization of vacuum membrane distillation module for low-cost water production. *Desalination* 339:1–9. <https://doi.org/10.1016/j.desal.2014.02.005>
 38. Anqi AE, Usta M, Krysko R et al (2020) Numerical study of desalination by vacuum membrane distillation transient three-dimensional analysis. *J Membr Sci* 596:117609. <https://doi.org/10.1016/j.memsci.2019.117609>
 39. Imdakm AO, Matsuura T (2004) A Monte Carlo simulation model for membrane distillation processes: direct contact (MD). *J Membr Sci* 237:51–59. <https://doi.org/10.1016/j.memsci.2004.03.005>

40. Phattaranawik J, Jiratananon R, Fane AG (2003) Effect of pore size distribution and air flux on mass transport in direct contact membrane distillation. *J Membr Sci* 215:75–85. [https://doi.org/10.1016/S0376-7388\(02\)00603-8](https://doi.org/10.1016/S0376-7388(02)00603-8)
41. Mengual JI, Khayet M, Godino MP (2004) Heat and mass transfer in vacuum membrane distillation. *Int J Heat Mass Transf* 47:865–875. <https://doi.org/10.1016/j.ijheatmasstransfer.2002.09.001>
42. Zhao LH, Lu XL, Wu CR et al (2015) Flux enhancement in membrane distillation by incorporating AC particles into PVDF polymer matrix. *J Membr Sci* 500:46–54. <https://doi.org/10.1016/j.memsci.2015.11.010>
43. Zhao LH, Wu CR, Liu ZY et al (2016) Highly porous PVDF hollow fiber membranes for VMD application by applying a simultaneous co-extrusion spinning process. *J Membr Sci* 505:82–91. <https://doi.org/10.1016/j.memsci.2016.01.014>
44. Zhang YG, Peng YL, Ji SL et al (2016) Numerical simulation of 3D hollow-fiber vacuum membrane distillation by computational fluid dynamics. *Chem Eng Sci* 152:172–185. <https://doi.org/10.1016/j.ces.2016.05.040>

Publisher's Note Springer Nature remains neutral with regard to jurisdictional claims in published maps and institutional affiliations.